JOURNAL OF GEOPHYSICAL RESEARCH: OCEANS, VOL. 118, 273–286, doi:10.1029/2012JC008154, 2013

Measurements of shoaling internal waves and turbulence in an estuary

Clark Richards,[1] Daniel Bourgault,[2] Peter S. Galbraith,[3] Alex Hay,[1] and Dan E. Kelley[1]

Received 20 April 2012; revised 21 September 2012; accepted 30 October 2012; published 30 January 2013.

[1] The shoaling of horizontally propagating internal waves may represent an important source of mixing and transport in estuaries and coastal seas. Including such effects in numerical models demands improvements in the understanding of several aspects of the energetics, especially those relating to turbulence generation, and observations are needed to build this understanding. To address some of these issues in the estuarine context, we undertook an intensive field program for 10 days in the summer of 2008 in the St. Lawrence Estuary. The sampling involved shore-based photogrammetry, ship-based surveys, and an array of moorings in the shoaling region that held both conventional and turbulence-resolving sensors. The measurements shed light on many aspects of the wave shoaling process. Wave arrivals were generally phase-locked with the M_2 tide, providing hints about far-field forcing. In the deeper part of the study domain, the waves propagated according to the predictions of linear theory. In intermediate-depth waters, the waves traversed the field site perpendicularly to isobaths, a pattern that continued as the waves transformed nonlinearly. Acoustic Doppler velocimeters permitted inference of the turbulent energetics, and two main features were studied. First, during a period of shoaling internal waves, turbulence dissipation rates exceeded values associated with tidal shear by an order of magnitude. Second, the evolving spectral signatures associated with a particular wave-shoaling event suggest that the turbulence is at least partly locally generated. Overall, the results of this study suggest that parameterizations of wave-induced mixing could employ relatively simple dynamics in deep water, but may have to handle a wide suite of turbulence generation and transport mechanisms in inshore regions.

Citation: Richards, C., D. Bourgault, P. S. Galbraith, A. Hay, and D. E. Kelley (2013), Measurements of shoaling internal waves and turbulence in an estuary, *J. Geophys. Res. Oceans*, *118*, 273–286, doi:10.1029/2012JC008154.

1. Introduction

[2] Recent advances in the understanding of nonlinear internal waves arising from field observations have focused on continental shelves, and reveal a complicated picture of the shoaling process and the effects on mixing and lateral transport of both fluid and turbulence. *Klymak and Moum* [2003] observed near-bottom waves of elevation on the Oregon continental shelf, with high values of turbulence dissipation within the waves. Another study by *Moum et al.* [2007], including time series and vertical profiles of turbulence, revealed that turbulence decayed more rapidly than the local buoyancy time scale, and concluded that turbulent fluid was transported within the wave cores and not left behind to decay. On the New Jersey shelf, shoaling nonlinear internal waves have been observed to undergo polarity reversal from waves of depression to waves of elevation [*Shroyer et al.*, 2009], while experiencing dissipative losses during propagation [*Shroyer et al.*, 2010a]. Vertical heat flux associated with the waves was observed to be an order of magnitude larger than the background, due to enhanced diffusivities at the pycnocline [*Shroyer et al.*, 2010b]. Farther inshore from the continental shelf, over a rough barrier reef, *Davis and Monismith* [2011] observed elevated near-bottom turbulence associated with passing internal waves, concluding that the waves significantly modified the structure of the turbulent bottom boundary layer on the reef.

[3] Given the strong stratification and large tidal currents in many estuaries, the transfer of energy from the mean flow to turbulence through internal waves has been suggested as being important to the overall energy budget [see, e.g., *Jay and Smith*, 1990; *Bourgault and Kelley*, 2003; *Groeskamp et al.*, 2011]. It is not clear that results from continental shelves will carry over to estuaries, because the latter tend to have different physical scales, background stratification, and flow fields. This provides a good incentive to undertake studies of internal waves and turbulence in estuaries.

[1]Dalhousie University, Halifax NS, Canada.
[2]Institut des sciences de la mer de Rimouski, Université du Québec à Rimouski, Rimouski, QC, Canada.
[3]Maurice-Lamontagne Institute, Mont-Joli QC, Canada.

Corresponding author: C. Richards, Woods Hole Oceanographic Institution, 86 Water Street, Woods Hole, MA 02543, USA. (crichards@whoi.edu)

2169-9275/13/2012JC008154

[4] In the St. Lawrence Estuary in Quebec, Canada, *Bourgault et al*. [2008] observed a series of upslope propagating waves using a vertical microstructure profiler, but measurement limitations prevented identifying the source of the turbulence. More recently, *Cyr et al*. [2011] found that boundary mixing was important in the decay of a cold intermediate layer in the lower St. Lawrence Estuary. The source of the boundary mixing, derived either from shoaling internal waves or bottom-boundary layer processes, is unknown.

[5] Field work related to boundary mixing in the St. Lawrence Estuary has identified a region in which high-frequency internal waves propagate perpendicular to isobaths. Wave generation is hypothesized to occur within approximately 10 km of the shoaling site, eventually permitting measurements of the full evolution from generation to dissipation. Experience at the field site began with an exploratory study [*Bourgault and Kelley*, 2003] that led to a repeating field program which offered insights on internal wave shoaling [*Bourgault et al*., 2005, 2007] and reflectance [*Bourgault and Kelley*, 2007]. These in turn led to the data analysis techniques of *Mirshak and Kelley* [2009]. A recent focus has been on the breaking phase of internal waves, including bolus production and turbulence [*Bourgault et al*., 2008]. This last issue, which we will denote generally as the "dissipation phase", is the focus of the present paper and is of particular interest from the viewpoint of parameterizing the role of internal waves in coastal mixing.

[6] These previous studies indicated a clear need for further turbulence measurements. A field program conducted at the site during the summer of 2008 included ship-based sampling, shore-based photography, and mooring time series. The dense mooring array contained both conventional and turbulence-resolving sensors.

[7] This paper presents the first results from the 2008 field campaign, beginning with a description of the experiment and the background oceanographic conditions relevant to our study (section 2). We then present a brief description of the methods used (section 3), followed by results related to measurements of internal waves and turbulence (section 4). A discussion on the source of turbulence measured within shoaling waves is then given (section 5), followed by conclusions (section 6).

2. Experiment and Background Conditions

[8] Figure 1 shows the study region and mooring locations, located along a gently sloping bottom (between 0.5 and 2°) on the flank of Île aux Lièvres, in the upper St. Lawrence Estuary. Figure 2, a georectified shore-based photograph taken 10 days before the start of the experiment, provides context for the interest in internal waves at this location. Visible in the image are at least five groups of wave-like surface signatures, seen from time lapse animation to propagate in the directions indicated by the arrows. The waves in group "1" were propagating toward the shore of Île aux Lièvres, refracting as they shoal. Figure 2 provides good motivation to study internal wave shoaling in this area, given the complexity of the wave field and the interaction with the bathymetry. The 2008 field site is located to the north of the camera's field of view, which was obscured by trees in that direction.

[9] Moorings were deployed from 25 June to 4 July 2008 in a mostly across-channel configuration, consistent with previously observed wave propagation directions [*Bourgault and Kelley*, 2003; *Bourgault et al*., 2007]. Mooring locations, water depths, instrument heights, and sampling parameters are listed in Table 1. Moored instruments consisted of acoustic Doppler profilers (ADPs), acoustic Doppler velocimeters (ADVs), and temperature-depth recorders (TDRs). The x and y position is indicated by a terrain-based coordinate system with origin on the island at the location of a camera system (47°52′31.75″N; 69°43′1.16″W), and the x-axis rotated 31.5° clockwise from east. Instrument depths were determined by a tidal harmonic analysis for every instrument that contained a pressure sensor.

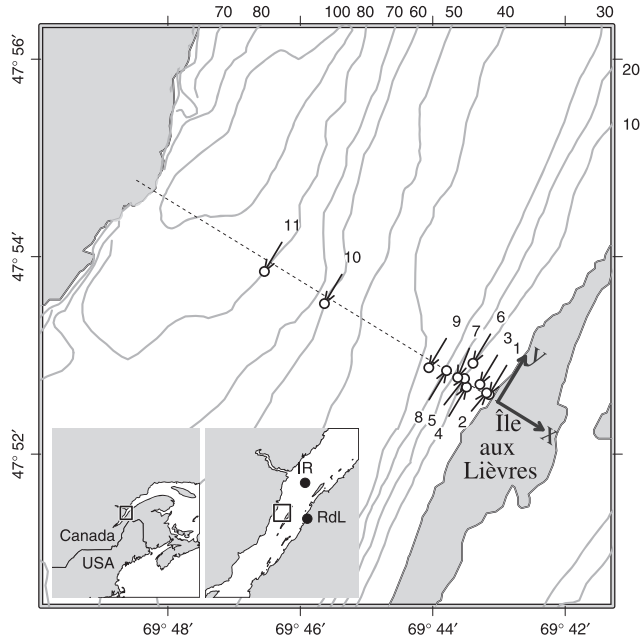

Figure 1. Study region, showing 11 moorings near Île aux Lièvres, an island in the St. Lawrence Estuary (insets). Contours of depth in meters are labeled outside the frame. The dashed line indicates the orientation of a time-lapse camera system set up on the island to overlook the moorings. The axes of an xy coordinate system centered on this camera are drawn to indicate 1 km distance. Locations labeled on the medium-scale inset include Île Rouge (IR) and Rivière-du-Loup (RdL).

[10] Moorings M01 through M09 were deployed along the slope to capture waves during various stages of disintegration and possibly track features over time and space. Moorings M10 and M11 were deployed on streamlined underwater buoyancy systems (SUBS) in the deep channel to capture wave propagation in the far field (not discussed here). Moorings M05, M07, and M08 were multi-instrument "pods", containing an upward-looking ADP, and at least one ADV. Pods M05 and M07 contained downward looking ADPs, to sample the near-bottom current in high resolution (4 and 5 cm bins). Mooring M08 also contained a line of 7 TDRs.

[11] Ship-based sampling was performed throughout the experiment, from a variety of different platforms. The R/V *Coriolis II* was used on 25–26 June to deploy moorings and perform a hydrographic survey of the region using a conductivity-temperature-depth profiler (CTD). During daylight hours from 27 June to 2 July, ship-based sampling was performed using the R/V *Lampsilis* (CTD and vessel-mounted ADP) and the R/V *Merlu* (towed echosounder and ADP).

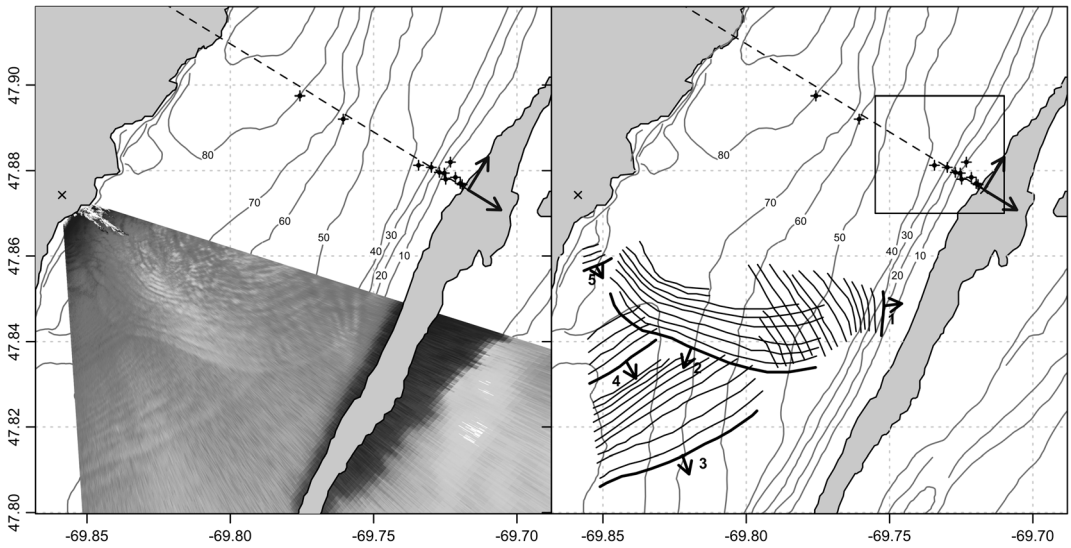

Figure 2. Sea-surface patterns observed on 15 June 2008 13:47:09 UTC (during the flood phase of the tide, about 2 h after low water, 10 days before the beginning of the field experiment) from a location on the northern shore indicated by the cross. Camera elevation is 308 m. The complicated wave field is revealed by several distinct groups of internal waves, moving in different directions. The box around the field site indicates the region within which shore-based photography was used during the experiment.

[12] In addition to the mooring and ship data, shore-based photogrammetry was used to obtain georectified images of the sea surface, including surface signatures of the propagating internal waves.

2.1. Background Conditions

2.1.1. Meteorology

[13] Meteorological data (wind speed and direction) were obtained from a station on Île Rouge (see Figure 1), a small treeless island about 25 km downstream from the field site. The Île Rouge station lacked air temperature measurements for the period of interest, so these were obtained from Rivière-du-Loup, about 15 km to the southeast. Although wind stress driven turbulence and surface heat flux are potentially important to the estuarine dynamics overall, they are not considered here because analysis shows no obvious correlation between turbulence dissipation rates and wind stress or air temperature.

2.1.2. Tides

[14] Tides at the field site consist of a mixed diurnal/semidiurnal tide, with a spring/neap cycle. Sampling began about halfway through the neap cycle, progressing toward the

Table 1. Moorings and Instruments From the 2008 Field Program[a]

Name	x (m)	y (m)	Sensor	Freq	δt (s)	δz (m)	HAB (m)	Water Depth (m)
M1	–208	34	TDR	NA	1	NA	0.20	2.0
M2	–265	35	Vector	6 MHz	0.25	NA	0.97	3.0
M3	–457	106	ADV	10 MHz	0.1667	NA	0.82	6.7
M4	–646	–69	ADCP	1200 kHz	10	0.5	0.40	11.9
M5	–761	49	ADP	1.5 MHz	20	1	0.86	18.3
			ADV	10 MHz	0.1	NA	0.65	
			Vector	6 MHz	0.125	NA	0.98	
			Aquadopp	2 MHz	10	0.04	1.05	
M6	–775	376	ADCP	600 kHz	10	1	0.40	20.5
M7	–881	–1	ADCP	1200 kHz	10	0.5	0.97	23.3
			Vector	6 MHz	0.125	NA	0.37	
			PCADP	1.5 MHz	10	0.04	1.08	
M8	–1127	–1	ADP	1.5 MHz	20	1	0.45	32.9
			ADV	10 MHz	0.1	NA	0.58	
			Vector	6 MHz	0.125	NA	0.98	
			TDR chain	NA	1	NA	NA	
M9	–1440	–128	ADCP	600 KHz	10	0.5	0.57	39.7
M10	–3742	–126	ADCP	300 kHz	10	1	10.0	67.6
M11	–5019	–201	ADCP	300 kHz	10	1	31.9	84.5
			S4	NA	60	NA	9.5	

[a]The x and y positions are with respect to axes centered at 47°52′31.75″N, 69°43′1.16″W, with the x-axis rotated 31.5 degrees clockwise from east. "ADV" refers to acoustic doppler velocimeters (including units called "ADV" manufactured by Sontek and called "Vector" manufactured by Nortek), "ADP" refers to acoustic doppler profilers (called "ADP" by Sontek, "ADCP" by Teledyne RDI, "PCADCP" by Sontek, and "Aquadopp" by Nortek), "TDR" refers to temperature-depth recorders manufactured by RBR, and "S4" Refers to S4 current meter manufactured by InterOcean. The TDR chain at mooring M08 consisted of seven units separated by a spacing of 4 m. See text for other details.

maximum spring tide. The tidal range was about 2.5 m during neap tides, increasing to 4.5 m during spring tides. Instantaneous currents reached ~3 m s^{-1} near the surface, as a result of the high tidal range and the superposition of the estuarine circulation. The tidal excursion was calculated to be about 5 km.

[15] To construct a "tidal clock" for use in analysis, the pressure measurements from all sensors were combined and fitted using a smoothing spline that eliminated features lasting less than about 2 h. From this signal, tidal phase (in radians) is calculated using

$$\phi(t) = \tan^{-1}\left(\frac{2\pi}{\tau_{M_2}}\frac{p_n}{\partial p_n/\partial t}\right), \quad (1)$$

where p_n is the demeaned pressure from the spline, $\partial p_n/\partial t$ is its time derivative, and τ_{M2} is the M_2 tidal period. A phase of 0 corresponds to maximum flood, while $\pm\pi$ corresponds to maximum ebb.

2.1.3. Hydrography

[16] The temperature-salinity relationship is shown in Figure 3, inferred from the CTD survey carried out with the R/V *Coriolis II* over a 30 h period in the region. There is a tight relationship between T and S. Most of the recording instruments sampled T but not S, so a regression relationship $S = S(T)$ was developed to infer salinity from temperature. Trials with different polynomial fitting functions led to the choice of a fourth-order polynomial of the form

$$S(T) = a_0 + a_1 T + a_2 T^2 + a_4 T^4, \quad (2)$$

where S is practical salinity. Coefficients were found to be: $a_0 = 32.25$, $a_1 = -0.6897^{\circ}C^{-1}$, $a_2 = -0.1068^{\circ}C^{-2}$, and $a_4 = 3.226 \times 10^{-4\circ}C^{-4}$ (residual standard error 0.179 on $>5 \times 10^4$ degrees of freedom; $R^2 = 0.9981$; $p < 2 \times 10^{-16}$ overall and for each term).

[17] Figure 3 also shows the mean density profile inferred from the CTD survey. The measurements were fitted to

$$\sigma_\theta = b_0 + b_1 z + b_2 \tanh\frac{z - b_3}{b_4} \quad (3)$$

using a nonlinear least-squares technique, yielding residual standard error 1.3 kg m^{-3} on $>5\times 10^4$ degrees of freedom; $p < 2 \times 10^{-22}$ for each b coefficient. The resulting standard residual of 1.3 kg m^{-3} represents approximately 10% of the range of σ_θ. Values for the coefficients in the fit are: $b_0 = 17.21$ kg m^{-3}, $b_1 = -0.03024$ kg m^{-4}, $b_2 = -4.572$ kg m^{-3}, $b_3 = -15.54$ m, and $b_4 = 13.20$ m.

[18] Using this relationship, a representative value of buoyancy frequency in the pycnocline is calculated to be $N_p = 0.060 \pm 0.002$ s^{-1}, where the $\pm$ value results from taking the standard errors in b_2, etc., as reported by the statistical procedure, and propagating them assuming independence [*JCGM*, 2008]. This analytical form of the density profile yields smooth vertical gradients, from which internal wave modes may be calculated. It should be noted that this mean profile is likely oversmoothed, due to spatial averaging and aliasing of tidal variations and high frequency heaving of isopycnals.

2.1.4. Currents and Shear

[19] Phase-averaged current and the magnitude of the vertical shear for M07 are presented in Figure 4. The phase averaged shear magnitude was calculated as

$$< S >_{pa} = \left\langle \sqrt{\left(\frac{\partial u}{\partial z}\right)^2 + \left(\frac{\partial v}{\partial z}\right)^2} \right\rangle_{pa}, \quad (4)$$

where (u,v) are across- and along-shore currents (corresponding to the x and y axes) and $\langle . \rangle_{pa}$ represents phase averaging. For each M_2 cycle the velocities were interpolated to a common phase based on equation (1) (with maximum ebb corresponding to $\pm\pi$), which were then averaged over all cycles.

[20] Average currents are dominated by the tidal flow, so only the y-component is presented here. Average tidal currents reach ± 1.5 m s^{-1}, with some vertical structure throughout the tidal cycle. Vertical shear during the falling tide is dominated by near-bottom shear (~0.15 s^{-1}) and there is evidence of a near-surface shear layer as well. The ebb to flood transition tends to occur first at depth, leading to enhanced mid-water-column shear with a magnitude similar to that near the bottom. Averaged over all phases and depths, there is a background shear of approximately 0.07 s^{-1}. The bottom two panels in Figure 4 will be discussed in later sections.

[21] Time-mean currents near the island (M03 to M09) are everywhere positive (i.e., downstream). This is expected given the depth of the channel on the northern shore, where the subsurface upstream estuarine flow is concentrated, consistent with conceptual models [*Fischer et al.*, 1979] and other studies of the area [*Saucier and Chassé*, 2000]. Mean

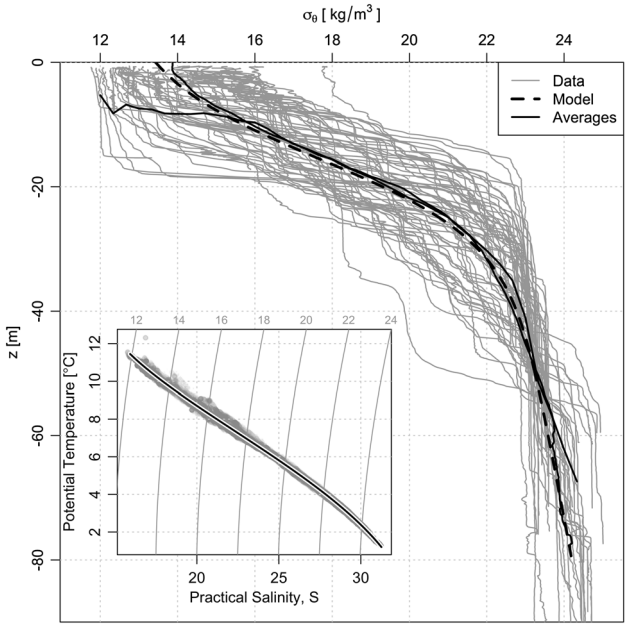

Figure 3. Vertical density structure in the region, as indicated by a CTD survey spanning the domain indicated in Figure 1 and covering 25 June through 26 June 2008. Gray lines indicate measured profiles, while the dashed black line is the result of a least-squares fit to a stratification model (see text), and the two solid black lines result from forming the mean density at depth, and mean depth at density. Inset is the temperature-salinity relationship. Measurements are indicated with grey dots, and the curve represents a least-squares curve fit.

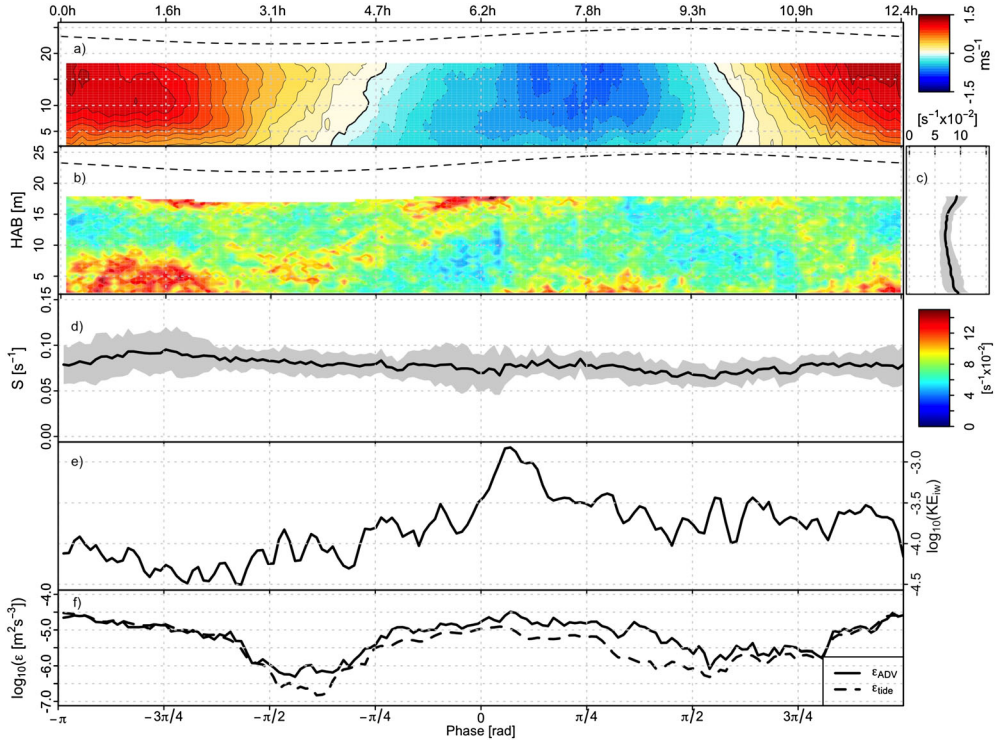

Figure 4. M07 phase-averaged (a) alongshore current, (b) vertical shear magnitude, (c) average shear profile, (d) depth averaged shear, (e) the logarithm of the kinetic energy proxy KE_{iw}, and (f) measured dissipation and a prediction from a tidal shear model (see sections 3.2 and 3.3). A phase of 0 corresponds to maximum flood, while $\pm\pi$ corresponds to maximum ebb. The dashed line in Figures 4a and 4b is the location of the surface. The contours in a represent 0.1 m s^{-1}, and zero is indicated by the thick line. For the depth- and phase-averaged shear in c and d the shaded regions represent the average shear $\pm$ the standard deviation. The times along the upper axis indicate hours in the M_2 tide.

currents at M10 and M11 (in ~60 and 80 m of water respectively) show a flow reversal at depth.

3. Methods

3.1. Shore-based Photogrammetry

[22] In the right conditions, internal waves have signatures at the surface in the form of alternating dark and light bands [*Wang and Pawlowicz*, 2011]. Shore-based photogrammetry has been successfully applied in the study region previously [*Bourgault and Kelley*, 2003], although never coincident with in situ data as during this field campaign. Two cameras were used, with their fields of view overlapped by a few degrees. The images were georectified with the method described by *Bourgault* [2008]. Figure 5 shows an example image, from 1 July, where a series of bands was observed propagating toward the shore.

[23] Images from Île aux Lièvres were collected at 45 s intervals on 1 July, and 30 s intervals on 2 July, from an elevation of 35 m. Poor weather conditions (rain, strong winds, and a choppy surface) prevented the use of photogrammetry on other days. Images were rectified using 30 ground control points collected using the R/V *Merlu* within the region of the moorings. Image resolution was 3888 × 2592 pixels, leading to maximum pixel dimensions (and hence position uncertainty) of 20 m for locations approximately 2 km from the camera (decreasing to 1 m for locations 250 m from the camera).

3.2. Internal Waves

[24] To construct a time series of internal-wave activity at each mooring, we used a proxy for the kinetic energy, based on the depth-averaged vertical velocity. In the presence of large background flow and shear, internal waves are more easily isolated from the vertical velocity field than from the horizontal. The depth-averaged vertical wave velocity w_{iw} was calculated by applying a second-order forward-and-reverse band-pass Butterworth filter, with 6 dB cutoff frequencies of $10^{-1}N_p$ and $10^{1/2}N_p$, where N_p is the average pycnocline buoyancy frequency (section 2.1.3). A proxy for internal wave kinetic energy was then calculated as

$$KE_{iw} = \frac{1}{2}\langle w_{iw}^2 \rangle_{lp}, \tag{5}$$

where $\langle . \rangle_{lp}$ is a low-pass filter with cutoff $10^{-1}N_p$.

3.3. Turbulence Dissipation Rates

[25] Near-bottom turbulence dissipation rates were calculated from the high-frequency velocity measured by the ADVs using the inertial dissipation method [see, e.g., *Huntley*, 1988; *Green*, 1992; *Kim et al.*, 2000]. Assuming a balance between shear production of turbulence and viscous dissipation, a spectrum of the three-dimensional velocity variations will contain an inertial subrange provided there is sufficient scale separation between the two processes.

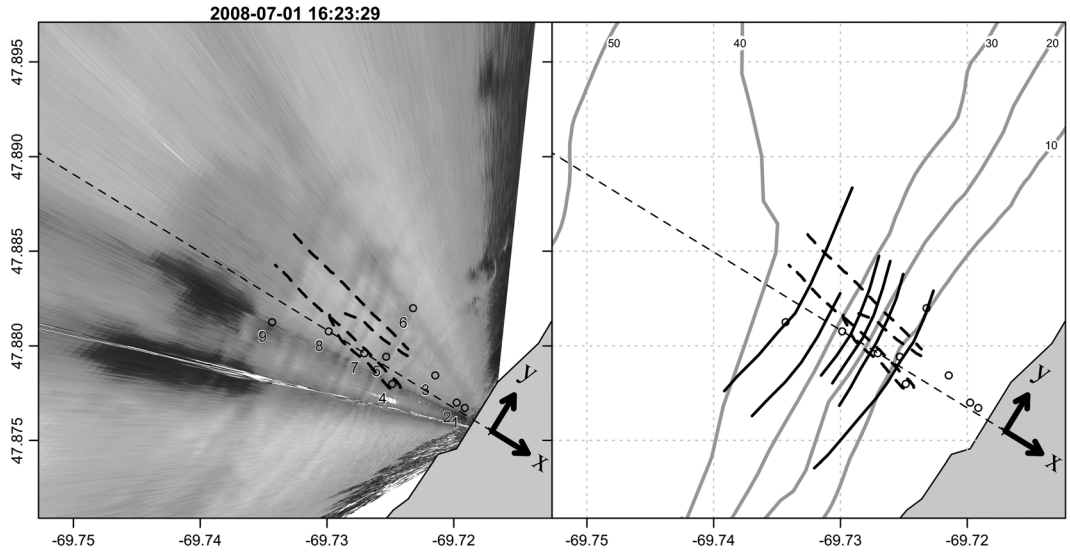

Figure 5. Example georectified image, from 1 July 16:23:29 UTC. (left) The rectified image plotted with the coastline, coordinate system, and the moorings. Camera elevation is 35 m. Bands of alternating brightness are surface signatures of internal waves, propagating toward the coastline. (right) The same view, but with the wave front positions plotted over the bathymetry to show orthogonality of the wave propagation direction to the coast. The thick dashed line corresponds to the echosounder transect from Figure 8. The *xy* axes are drawn to indicate a 250 m distance.

[26] In practice, turbulence measurements generally make use of spectra calculated from a single velocity component, as a function of the wave number in the direction of the mean flow k_1. In this case the energy spectrum can be written in a one-dimensional form (using the notation of *Huntley* [1988]) as

$$\Phi_{ii}(k_1) = \alpha_i \varepsilon^{2/3} k_1^{-5/3}. \tag{6}$$

[27] Here i corresponds to the direction of the turbulent fluctuations (with $i=1$ for longitudinal and $i=3$ for transverse), and α_i is the corresponding one-dimensional Kolmogorov constant. Given isotropic turbulence, $\alpha_3 = \frac{4}{3}\alpha_1 = 0.69$ [*Green*, 1992; *Sreenivasan*, 1995].

[28] A wave number spectrum $\Phi_{ii}(k)$ is developed from the frequency spectrum $\phi_{ii}(f)$ using Taylor's frozen turbulence hypothesis that the turbulence is advected past the sensor by the mean flow as a frozen eddy field, giving [*Tennekes and Lumley*, 1972; *Monin and Yaglom*, 1975],

$$\Phi_{ii}(k) = \frac{\varphi_{ii}(f)}{2\pi/\bar{U}}, \tag{7}$$

where $\bar{U} = \left(\bar{u}^2 + \bar{v}^2\right)^{1/2}$, (u,v) are the two horizontal velocity components, $k = 2\pi f/\bar{U}$ is the wave number, and the bar represents the mean over the time period used for the spectrum. *Huntley* [1988] suggests that this assumption is valid provided $k\Phi_{ii}(k)/\bar{U}^2 \ll 1$.

[29] In this study, we used the spectrum of the vertical velocity component ($i=3$) to estimate ε, for two reasons. First, because of the geometry of the transducer and receiver in the ADVs, the noise floor of the vertical component of velocity at high frequencies is lower than for horizontal velocities. Second, when wave and mean flow conditions are combined, the vertical velocities will be less contaminated by wave motion in the inertial subrange [*Stapleton and Huntley*, 1995]. Spectra were computed from the raw periodogram using 1 min intervals, and fit to the functional form in log-space. The fit procedure and quality control tests are discussed in Appendix A.

4. Results

4.1. Dissipation

[30] In addition to the quality controls applied to the dissipation measurements, it was found that erroneous values of ε (perhaps caused by vortex shedding from other instruments on the frame) were well correlated with the orientation of the frame on the bottom and the direction of mean flow. This suggests that flow contamination affected the velocimeter-derived dissipation measurements, which were then discarded for a range of suspect background flow angles.

[31] The relationship of ε to U_f^3 for the M05 Nortek Vector is shown in Figure 6, where U_f is a 30 min low-pass filtered velocity representative of the longer time scale forcing expected for a tidal bottom boundary layer. The overall characteristics for the other instruments are similar, with most of the points lying along a line with slope equal to 1 in log-space. In an unstratified channel of depth H, shear production of turbulence will be proportional to U^3/H [see, e.g., *Taylor*, 1920], where U is the horizontal velocity magnitude at some height above bottom, and the constant of proportionality corresponds to an appropriate drag coefficient C_D. Assuming a local balance between production and dissipation, ε should scale similarly. Overall the data in Figure 6 agree with the $\varepsilon \propto U_f^3$ model; however, there is a significant amount of scatter around this line. At low velocities, the measured dissipation is at times more than 2 orders of magnitude higher than predicted, which suggests that there are

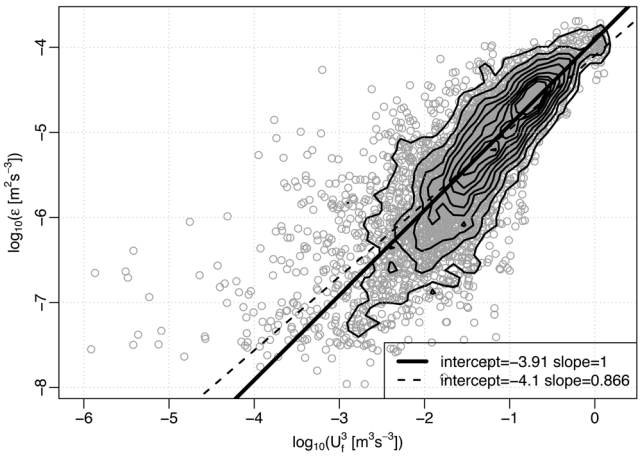

Figure 6. Comparison between ADV-derived U_f^3 and ε for the Nortek Vector at M05. The individual points are plotted as grey circles, while the contours indicate data density (decreasing from 90% to 10%). The solid line is the result of a linear fit with a slope of 1, and the dashed line the result of a linear fit with slope unconstrained. Only points which passed all quality control tests are displayed.

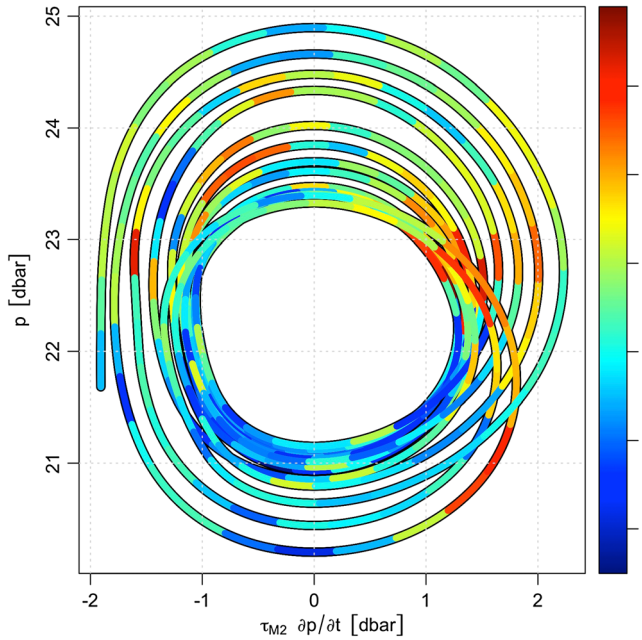

Figure 7. Wave energy proxy KE_{iw} at M07. The axes are based on the pressure spline, with the multiplication by M_2 tidal period yielding a circular trace for a sinusoidal M_2 tide. The colors indicate the base-10 logarithm of wave energy proxy, in arbitrary units, averaged in 30 min bands. Deep blue indicates low values and deep red indicates high values.

processes that increase ε at low tidal velocities that are beyond the values associated with tidal shear scaling.

4.2. Wave Arrivals

[32] Internal wave energy at the field site was binned into 30 min averages and plotted as a function of tidal phase, using a "phasor"-type plot, where the (tidal) pressure is plotted against its time derivative, normalized using the M_2 period (see Figure 7). Much of the internal-wave energy appears during the rising tide (on average twice as much as during the falling tide), consistent with previous observations in this region [*Bourgault and Kelley*, 2003; *Mirshak*, 2008], and suggesting a tidal generation mechanism. There are indications of internal waves at other times, but they do not occur consistently on each tidal cycle. The source of these other waves may be related to the signatures seen in Figure 2, but here we focus on the waves that appear to be phase-locked with the M_2 tide.

4.3. 1 July Wave Shoaling Event

[33] To highlight the synthesis of the mooring data, ship transects, and shore-based photogrammetry, a focus period was chosen on 1 July, between the hours of 15:00 and 19:00 UTC. This time was during a rising tide, when waves are most likely to be observed, motivated by the phase-averaged wave proxy and dissipation time series in Figures 4e and 4f (see also Figure 7). An example image from the shore-based photogrammetry is presented in Figure 5, showing the surface signatures of at least six waves propagating toward the shore. A second focus time was chosen during the ebb phase of the tide to represent low internal wave conditions (based on Figures 4e and 4f). The focus periods had weak winds ($<$2–3 m s^{-1}) and minimal surface waves ($<$0.1 m).

[34] Figure 8 represents a "snapshot" of the water column structure obtained with the towed echosounder near the x-axis line (see Figure 5). The vertical profile of σ_θ inferred from the TDRs using the TS relationship at M08 suggests that the high backscatter layer at about 25 m depth corresponds to the pycnocline, and is therefore the location of maximum vertical internal wave displacement. Visible in Figure 8a are: a wave undergoing transition from a wave of depression to a wave of elevation ($x \approx -1250$ m), a wave of elevation ($x \approx -1100$ m), and a series of upslope propagating wave or bolus-like features (between $x \approx -1000$ and $x \approx -800$ m, and perhaps even shallower). The locations of the moorings show that our experimental design is well positioned to sample the waves at each phase of their transformation over the shoaling bottom.

[35] The echosounder panels in Figure 8 (Figures 8a, 8c, 8e, and 8g) show the evolution of the shoaling waves over a time period that spans 16:30 to 16:55 UTC. The vertical velocity measured by the ADCP at M07 is plotted to the right of each transect, for a 10 min interval centered on the time the ship passed the mooring. Together, the two data sets highlight the nonlinear evolution of the shoaling waves. In Figures 8–8b and 8c–8d, M07 is within the pycnocline region, and the wave signals observed by the profiler are strongly nonlinear (note the large vertical velocities, with the maximum speeds close to the bottom). In the transects plotted in Figures 8e–8f and 8g–8h, M07 is below the main pycnocline (as indicated by the backscatter), and the maximum vertical velocity signals are correspondingly higher in the water column and less intense. Tracking individual features in the echosounder transects from offshore to onshore highlights the cross-estuary transformation of a single wave. Note the feature identified by the inverted triangle, which transitions from a broad wave of elevation in Figure 8a to a narrow, highly nonlinear bolus by Figure 8g.

[36] Figure 8i shows the dissipation measured by the ADVs at M05 and M07. Along with the change in the wave properties

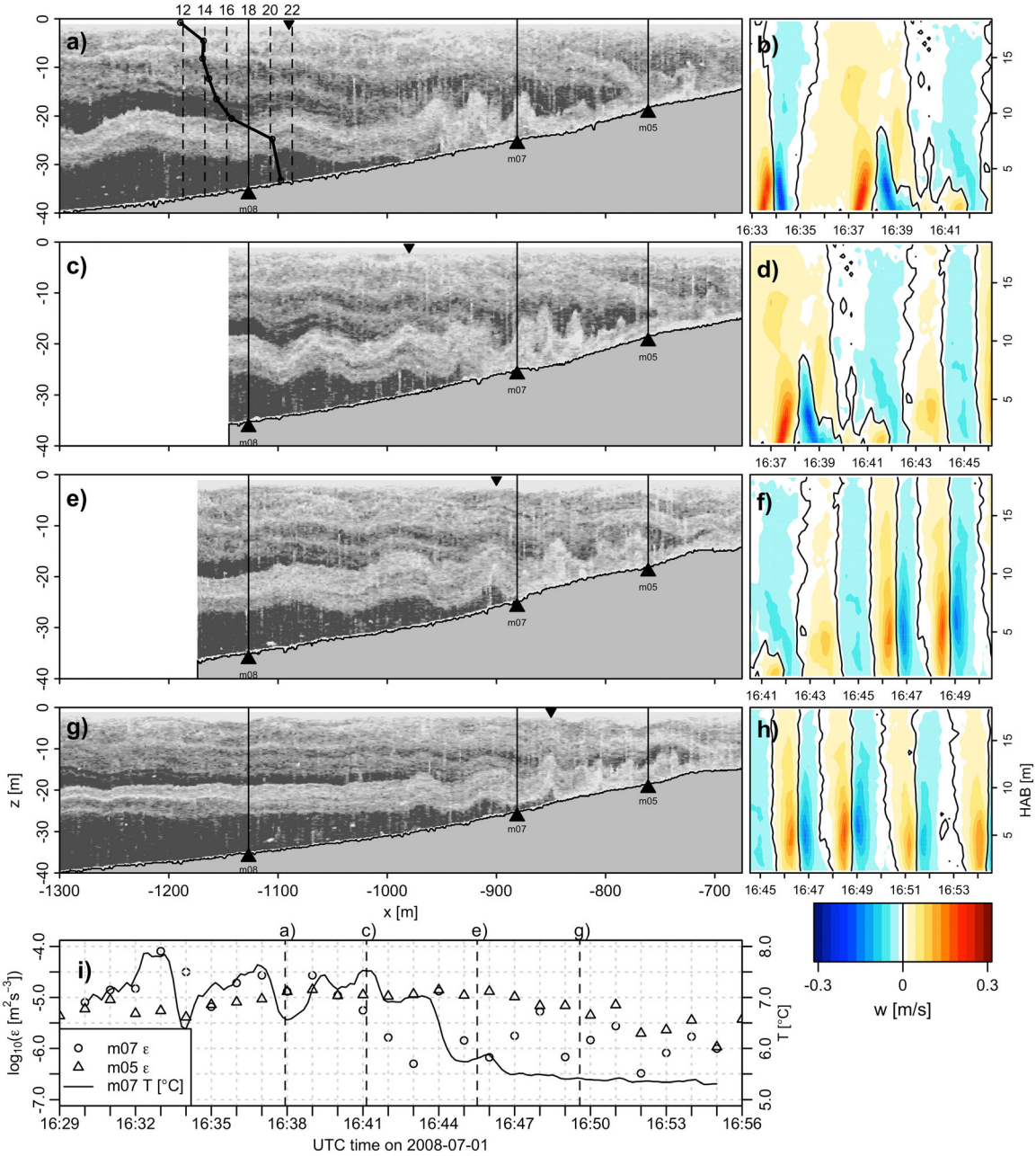

Figure 8. (a, c, e, and g) Towed echosounder transects along the mooring line, highlighting the evolution of shoaling internal waves. The distance along the *x*-axis is indicated along the bottom. The mooring locations are marked by the dark triangles and vertical lines, and the inverted triangles at the top of each transect identify the location of a wave feature discussed in the text. The vertical σ_θ profile at M08 is an instantaneous density profile calculated using the TDRs along with the TS relationship. Values are indicated by the dashed lines, in 2 kg m^{-3} increments from 12 to 22 kg m^{-3}. (b, d, f, and h) The vertical velocity measured by the M07 ADCP for a 10 min period centered on the time the ship passed the mooring. (i) A time series of the dissipation measured at M05 and M07, along with the temperature measured by the M07 ADCP.

observed at M07 during shoaling, there is a corresponding drop in the level of inferred dissipation. The drop in dissipation at M07 can also be seen to coincide with a decrease in bottom temperature at this location. This observation supports the view that the change in depth of the pycnocline has an effect on the wave properties observed at the mooring.

[37] The three velocity components, vertical shear, acoustic backscatter, and temperature are presented for the M07 ADP in Figure 9, showing a train of 5–6 waves of elevation (or boluses) passing the mooring during a 30 min period. The waves show strong onshore and vertical velocities (~0.5 and 0.25 m s^{-1}, respectively), and the vertical shear is dominated by the high-frequency wave contribution. Acoustic backscatter suggests significant resuspension of sediments consistent with other studies [*Quaresma et al.*, 2007], although this was not verified here with in situ data. The

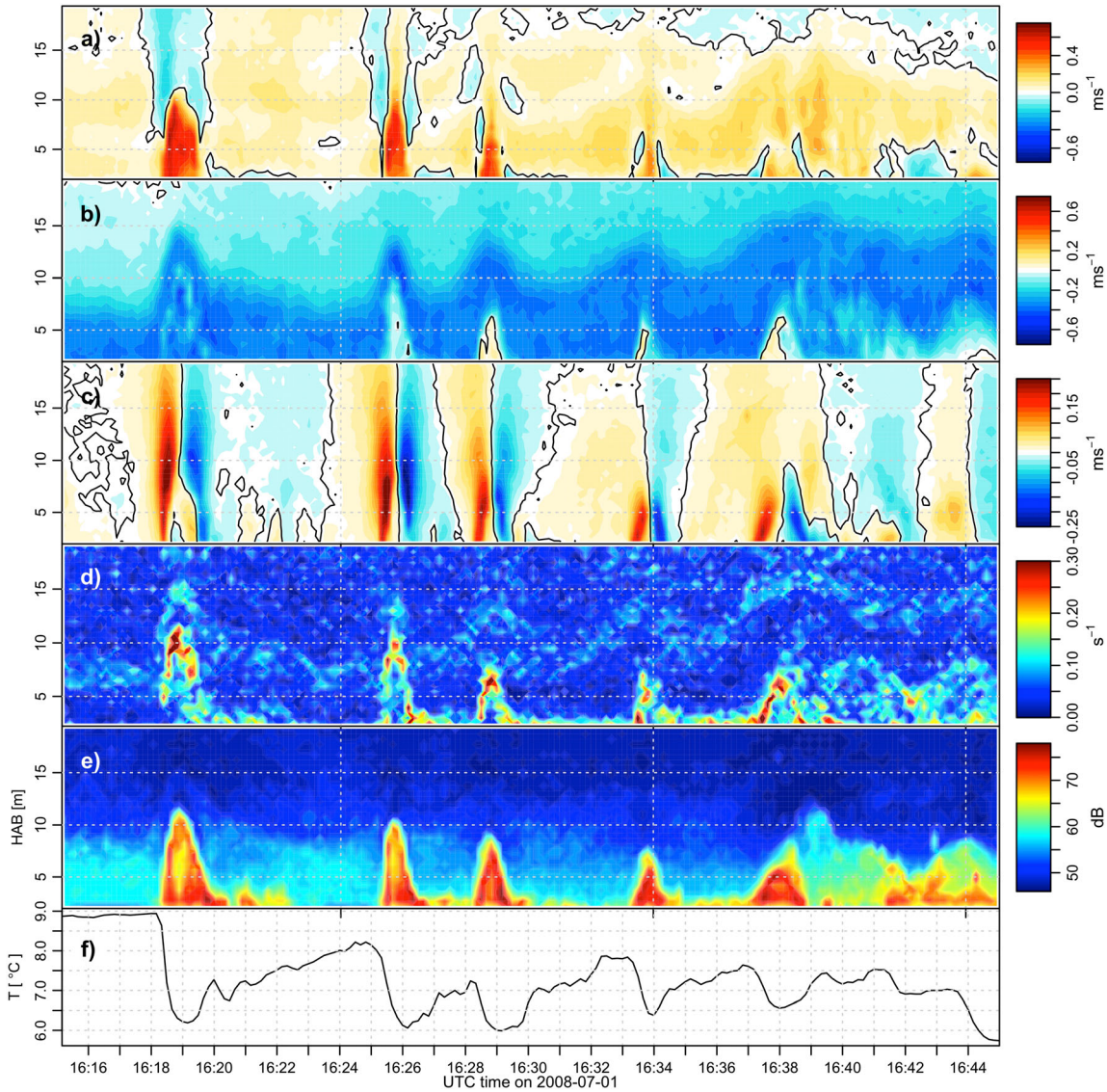

Figure 9. A 30 min segment of a wave shoaling event on 1 July as measured by the M07 ADP, showing (a) onshore velocity, (b) alongshore velocity, (c) vertical velocity, (d) magnitude of the vertical shear of the horizontal current, (e) acoustic backscatter, and (f) bottom temperature. The black line in (a), (b), and (c) indicates the zero contour.

temperature record shows pulses of cold, dense water, indicating possible horizontal transport of fluid within trapped cores [*Lamb*, 2003].

[38] To highlight the time dependence of features observed in the georectified images acquired on 1 July, the pixels located along the *x*-axis were extracted to create a distance-versus-time representation, presented in Figure 10. The image uses a nonlinear grayscale mapping to reveal features. Each column in the image was adjusted to have equal average brightness, removing the effects of varying background lighting conditions.

[39] Plotted in this way, propagating features can be identified as sloped bands, with their shoreward component of propagation speed indicated by the slope. To provide a reference, the mean vertical density profile was used in a calculation of the phase speed of internal wave modes [see e.g., *Gill*, 1982]. The solid black line beginning around 15:00 UTC indicates the path that would be taken by a linear mode-1 internal wave for the stratification shown in Figure 3, using the water depths of the field site approximated with a quadratic distance-depth model.

[40] Plotted overtop of the image at the positions of the moorings are the depth-averaged vertical velocities measured by the ADPs. Matches between the surface features and the velocity traces, combined with the reasonably good agreement between the observed and modeled phase speeds, especially in deeper water, suggests that the features correspond to passing internal waves.

[41] The correspondence of the observed surface signatures with internal wave signals from Figure 10 facilitates the extraction of the wave propagation direction from the time series of georectified images (Figure 5). Determining wave direction in this manner eliminates the need for more complicated techniques using the moored ADPs

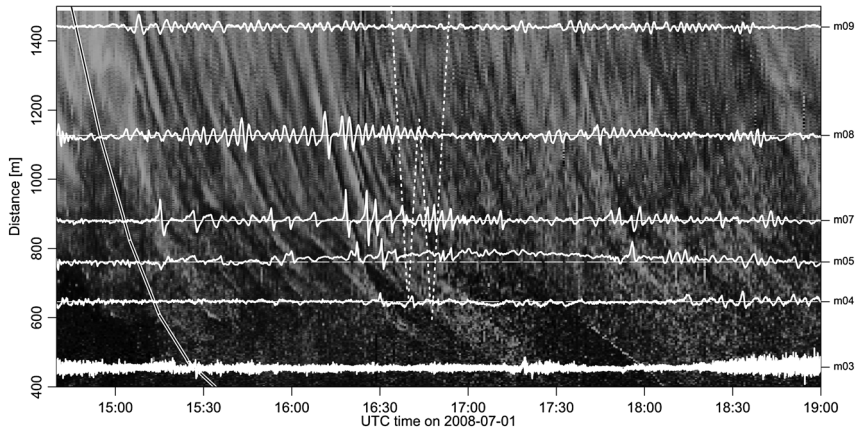

Figure 10. Surface brightness observed by the island-based camera, restricted to the line of pixels lying along the *x*-axis. Plotted overtop of the image are the depth-averaged vertical velocities *w* which show strong correlations with the propagating surface features. Note also the decrease in amplitude as the waves propagate into increasingly shallower water, indicating a loss of energy as they shoal. The vertical scale is arbitrary, but consistent between moorings. The solid black line is a model based on the mode-1 internal wave phase speed as a function of depth, and the dashed white lines indicate the locations of the echosounder transects in Figure 8.

[see, e.g., *Scotti et al*., 2005; *Mirshak and Kelley*, 2009]. The alignment of the observed wave crests with the bathymetry, and the extent of the crest along the *y*-axis (>1 km) supports the treatment of the waves and the shoaling process as two-dimensional [*Bourgault et al*., 2005, 2007].

[42] To separate the influence of the tides and internal waves on the dissipation rate, we used the tidal shear scaling presented in section 4.1. Time series of ε measured at M05 (from the Nortek Vector) are shown in Figure 11, for the two focus periods. In the upper panels, the dissipation predicted by the scaling is indicated by the gray line, using $C_D = 3 \times 10^{-3}$ for U measured 1 m above the bottom [*Soulsby*, 1997], and a 30 min cutoff low-pass filtered horizontal velocity. The bottom panels show the time series of internal-wave energy proxy. The ε results on the left hand side, during the period of low internal-wave activity, show good agreement with the tidal dissipation model (root mean square deviation of the logged time series of 0.35). During the period of high internal-wave activity (on the right), the measured dissipation is at times several orders of magnitude greater than that predicted by the model (root mean square deviation of the logged time series of 1.03). The highest dissipation rates measured by the ADV during the wave

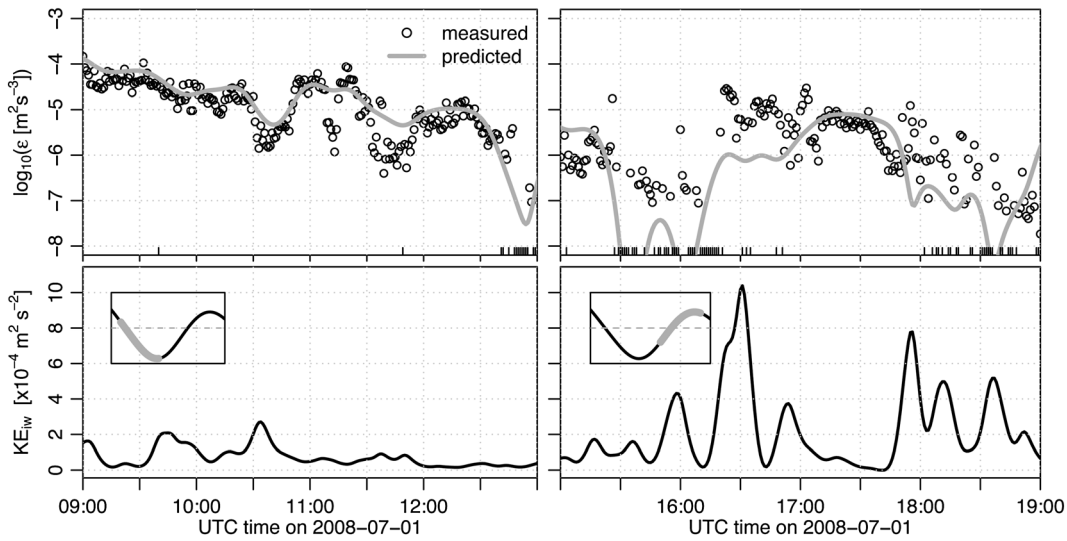

Figure 11. Dissipation rates inferred by the Nortek Vector at M05 (circles) and predicted by $C_D U_f^3 / H$ (gray line) for the two focus periods. Bottom panels show internal-wave activity over the same times, highlighting the periods of low (left) and high (right) internal-wave energy. The phase of the tide is plotted in the inset. The ticks along the bottom of the upper panels indicate times where dissipation values are missing due to the quality control tests.

passage are similar in magnitude to those observed during the maximum falling tide ($\varepsilon = 5 \times 10^{-5}$ m^2 s^{-3}).

5. Discussion

[43] Our measurements indicate a correlation between wave passage and elevated turbulence. Two mechanisms might explain such a correlation. One explanation may relate to vertical or horizontal advection, with waves heaving a near-bottom turbulent boundary layer into the sensing region, or with turbulence being carried laterally in trapped cores. Another explanation may relate to local production of turbulence, with waves producing turbulence through shear instabilities or bottom boundary layer processes. We take these two mechanisms in turn, beginning with vertical advection, keeping in mind that it is possible that more than one mechanism may contribute to the observed turbulence at any given time.

[44] While observing similar waves with a vertical microstructure profiler, *Bourgault et al.* [2008] were unable to determine if observed values of high dissipation were inherent to the waves or resulted from a heaved bottom boundary layer. They speculated that the boluses may act to inhibit turbulence, by increasing water column stability as they transport dense water up the slope. Their profiles did not extend all the way to the bottom, however, and this could have led to underestimation of the depth averaged water column

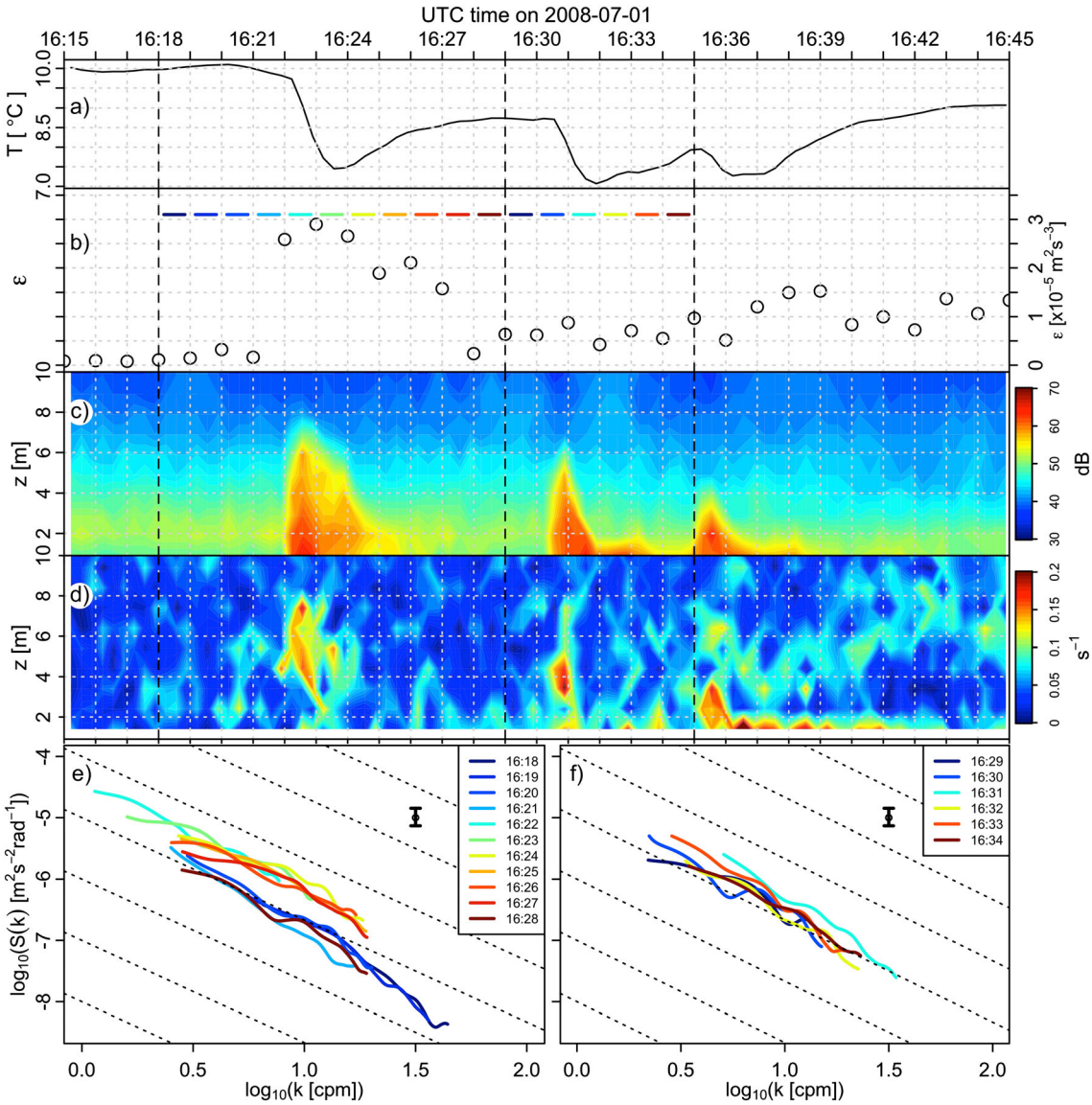

Figure 12. Three waves observed at M05, with (a) temperature from the ADP, (b) ε inferred from the Nortek Vector in 1 min segments, (c) ADP backscatter, (d) vertical shear magnitude in s^{-1}, (e) spectral evolution for the period from 16:18 to 16:29, and (f) spectral evolution for the period from 16:29 to 16:35. The colored segments in Figure 12b indicate the times for the individual spectra in Figures 12e and 12f, between the dashed vertical lines. The frequency spectra have been smoothed with a modified Daniell kernel with bandwidth 0.18 Hz and 95% confidence intervals are indicated by the vertical bar. The dotted lines indicate a slope of −5/3.

dissipation by orders of magnitude. In the present case, the near-bottom temperature record (Figures 9f and 12a) shows pulses of cold water associated with the waves. Comparing the observed temperature change (approximately 3°C) to the CTD profiles made to 80 m suggests advection of fluid up the slope by the waves. This in turn indicates that the fluid containing the turbulence likely did not originate near the bottom at the location of the sensor.

[45] Horizontal advection was advanced as a mechanism by *Moum et al*. [2007] in their study of shoaling waves on the Oregon shelf. Noting that the high dissipation associated with passing waves decayed in times much shorter than the buoyancy time scale, they concluded that the turbulence measured within the waves was transported along with them, rather than being left behind to decay. Dissipation time series for the leading wave presented in Figure 12 show a rapid increase in ε, followed by a slower decay, with a time scale of ~5–6 min. This is longer than the buoyancy period of about $2\pi/N \approx 40-100$ s (using either the ΔT from above, or the mean pycnocline N_p of 0.06 s^{-1}). Contrary to *Moum et al*. [2007], this suggests that the observed waves may leak turbulent fluid behind them. A possible explanation for the discrepancy with *Moum et al*. [2007] may be that the waves in the two studies were observed during a different stage of the shoaling process.

[46] The alternative limiting case is that turbulence is generated or dissipated entirely locally. It is possible to estimate the occurrence of turbulence generated by water column shear instabilities associated with the waves, using the density difference given above and the instantaneous values of vertical shear. From Figure 9d, instantaneous values of shear near the upper front face of the waves can be as high as 0.3 s^{-1}, over an interface about 2 m thick. Estimating $N^2 = -g/\rho_0(\partial\rho/\partial z) = 0.0206$ s^{-1} from the temperature difference leads to an estimate of the Richardson number of

$$Ri = \frac{N^2}{\mathcal{S}^2} \simeq \frac{0.0206}{0.3^2} = 0.23,$$

which is close to the critical value of 0.25. Given the uncertainties in the estimate (using $\Delta\rho = 4.3 \pm 0.3$ kg m^{-3}, $\Delta z = 2.0 \pm 0.5$ m, and $S = 0.3 \pm 0.05$ s^{-1} gives $Ri = 0.23 \pm 0.15$), this does not necessarily imply the onset of instability, but suggests that it may occur. The low *Ri* values are consistent with the *Bourgault et al*. [2008] observations of high values of ε at the leading face of some of the largest waves.

[47] An examination of the shape of successive velocity spectra during the focus period provides an indication of whether the observed turbulence is locally produced (Figure 12). Unlike the raw periodogram used to fit the functional form of the spectrum for determination of ε, here the frequency spectra have been smoothed using a modified Daniell kernel (with bandwidth 0.18 Hz). For the 1 July focus period, prior to wave arrival, the overall spectral slope is steeper than $-5/3$, indicating an excess of production versus dissipation, with more energy input to the lower wave numbers. Once the wave arrives at the ADV (16:22 UTC), the spectral level increases, and the shape approaches the $-5/3$ equilibrium form. During the decay, from ~16:24 to 16:28 UTC, the spectral level at lower wave numbers decreases relative to the higher wave numbers, indicating dissipation exceeding production. For this event, the waves represent a short-lived source of turbulent shear production, with local growth and decay of ε as a result. The results presented here pertain only to the 1 July event, though qualitatively similar patterns have been observed during wave events in other tidal cycles. A similar examination of the spectra during the following wave (Figure 12f) is not as conclusive, possibly due to the presence of turbulence left behind by the first, or by the enhanced near bottom shear evident in Figure 12d. Future studies of a similar nature, including more realizations to build statistics of the spectral changes, may reveal more details of the processes involved.

[48] We turn now to the broader energetic context. There was little evidence of internal-wave reflection, which suggests that the wave kinetic energy is either dissipated or transformed through mixing to potential energy. This scenario may be explored with a simple model of internal waves impinging on a linearly shoaling bottom. Taking W to be a characteristic vertical velocity scale, λ to be the wavelength, and L to be the distance over which the waves are destroyed, an estimate of the total energy density of the wave field is $E_w = \rho W^2\lambda^2/H^2$ (using the continuity equation and an assumption that $\lambda \gg H$). If all the wave energy is dissipated within the triangular cross section, one may infer a dissipation rate of $\varepsilon_w = cW^2\lambda^2/(2LH^2)$. For example, representative values from our observations ($c = 0.5$ m s^{-1}, $W = 0.1$ m s^{-1}, $\lambda = 100$ m, $L = 500$ m, $H = 30$ m) yield 6×10^{-5} m^2 s^{-3}. This value is roughly consistent with observations at mooring M05.

[49] The rate of transformation into potential energy will be proportional to the eddy diffusivity K_v. With the observed background value $N = 0.06$ s^{-1}, an estimate of the diffusivity is $K_v \sim \Gamma\varepsilon N^{-2} = 6 \times 10^{-3}$ m^2 s^{-1}, where $\Gamma \sim 0.2$ is a mixing efficiency [*Oakey*, 1982]. For the focus periods examined in Figure 11, representative dissipation rates during wave shoaling were about 6 times larger than values predicted by tidal shear scaling. If N^2 and mixing efficiency are constant over the period, K_v will be similarly enhanced. This "excess mixing" is caused by processes which will generally not be resolved within regional models, and would therefore be unaccounted for in a mixing budget of the domain.

6. Conclusions

[50] Results have been presented from an array of moored, underway, and shore-based instrumentation spanning a region of internal-wave dissipation in the St. Lawrence Estuary. The measurements reveal the cross-estuary transformation from weakly nonlinear waves in deep water, to highly nonlinear waves of depression as the shoaling bottom is approached. These waves of depression are then transformed into waves of elevation which propagate upslope as isolated boluses that decrease in amplitude with upslope distance.

[51] The overall wave field was revealed by photogrammetry and moored acoustic Doppler profilers. Internal-wave arrivals were generally phase-locked with the M_2 tide, suggesting a tidal generation mechanism. The waves propagated perpendicularly across isobaths, with speeds in deeper water that agree with the linear modal solution calculated using the mean hydrography.

[52] The turbulence dissipation rate, ε, was calculated from measurements made by ADV instruments. The effects of internal waves were studied by contrasting a particular time of high internal-wave activity with a time of low internal-wave

activity. It was found that ε is consistent with the predictions of a simple model of turbulence production by tidal shear but only when internal waves are absent. Maximum values of ε in low-flow, high internal wave periods were as large as the tidal shear values observed during a strong ebb tide.

[53] Near-bottom temperature signals indicate that the observed turbulence is unlikely to be caused by a heaved bottom boundary layer. Spectral shapes observed over the leading wave in a group suggest an initial excess of production versus dissipation as the wave arrives, followed by a period of decay characterized by excess dissipation. The time scale of the decay and the presence of turbulence after the wave passage both indicate that the waves may be leaving turbulent fluid behind them, at least at the level of the sensor. The evolving spectral signatures suggest that local generation of turbulence by the waves may occur in addition to advection of turbulent fluid within trapped cores.

[54] Further examination of these processes is warranted. In the meantime, a crude mixing budget suggests that mixing caused by internal waves should not be ignored in regional modeling studies. The rough diffusivity calculated in the previous section is similar to the value calculated by *Bourgault and Kelley* [2003], although it should be noted that neither calculation accounts for complications in the partitioning between kinetic and potential energies for nonlinear internal waves [*Moum et al*., 2007; *Lamb and Nguyen*, 2009]. Our ongoing work will attempt to address this and related issues involving energy fluxes.

Appendix A: Measuring ε and Quality Controls

[55] We fit the functional form of equation (6) to the raw periodogram of vertical velocity calculated using a 1 min period, which corresponds to either 480 or 600 data points, depending on the sampling rate (see Table 1). Tests were also done with times other than 1 min. The value of the slope, and the associated confidence interval of the fit were determined with a linear fit in log space using least squares. A "fit confidence" parameter was calculated as

$$QC_{\mathrm{ci}} = \left| \frac{m + 5/3}{c_i} \right|, \tag{A1}$$

where m is the slope determined from the least squares fit, and c_i is the 95% confidence interval for the fit. A value of $QC_{\mathrm{ci}} \leq 1$ indicates that a slope of –5/3 is within the 95% confidence interval of the fit. This approach is similar to one taken by *Feddersen* [2010] who rejected spectra if the best fit slope fell outside the range

$$m - 2\sigma_b - \beta < -5/3 < m + 2\sigma_b + \beta.$$

[56] Here σ_b is the standard error of the fit, and β is a factor allowing for some leeway given that the log spectra may not be Gaussian. Setting $\beta = 0$ corresponds to 95% confidence limits, much like the parameter QC_{ci} discussed above.

[57] In addition to the fit confidence parameter, a "fit anomaly" parameter QC_{fa} was calculated as the percent difference between the fit slope and –5/3, i.e.,

$$QC_{\mathrm{fa}} = \frac{5/3 + m}{5/3} \times 100. \tag{A2}$$

[58] A qualitative visual inspection of a large number of spectra believed to be turbulent led to a quality threshold $QC_{\mathrm{fa}} < 40$.

[59] Two other test parameters, related to the quality of the velocity data used to calculate the spectrum are the "amplitude" and "correlation" parameters, QC_{a} and QC_{c}.

[60] If too few scatterers are present within the ADV sample volume, the strength of the return signal will be close to the system noise, and the corresponding velocity measurement will be inaccurate. The noise level of a particular device varies between manufacturers, and even between instruments. To determine the noise level for the ADVs used here, we examined time series of backscatter amplitude from times when the instrument was known to be operating in air. *Elgar et al*. [2005] rejected any data runs if more than 0.81% of the values were below the determined threshold. *Feddersen* [2010] used a less conservative value of 10% to retain more data, but used further techniques to patch or interpolate data points flagged as suspect before calculating the spectrum. We rejected an entire spectrum if $QC_{\mathrm{a}} < 0.01$, based on *Elgar et al*. [2005], rather than use data replacement techniques [see, e.g., *Goring and Nikora*, 2002].

[61] The backscatter correlation for each beam, ranging from 0 to 100, is a measure of the degree of coherence between the return signal from pulse pairs used to determine the water velocity, and can be used to assess data quality [*Zedel et al*., 1996; *SonTek*, 2001]. Low correlation can be caused by the instrument operating in air, low SNR, and hardware malfunctions. In addition, highly turbulent or sheared flow can result in reflection of the pairs of pulses from different scatterers in the sample volume, also leading to low correlation. An along-beam correlation of 70% is recommended for high quality velocity estimation, though a minimum of 30% will still give accurate mean flows. *Elgar et al*. [2005] used a threshold of

$$\gamma_c = 0.3 + 0.4\sqrt{f_s/f_{\max}}, \tag{A3}$$

where f_{s} is the sampling frequency, and $f_{\max}$ is the maximum frequency of the instrument (e.g., 25 Hz for SonTek ADVs). For the ADVs used here, γ_{c} was 0.53 or 0.55, depending on the frequency (8 or 10 Hz). As with QC_{c}, we chose a conservative value of 0.01 (the spectrum was rejected if more than 1% of the values were below the cutoff).

[62] The frozen turbulence assumption leads to a final quality control check, QC_{ft}. After evaluating the mean value of $k\Phi/\bar{U}^2$, the spectrum is rejected if it is larger than 0.05.

[63] **Acknowledgments.** We would like to thank the two anonymous reviewers whose insightful comments greatly improved the manuscript. Contributions to the field work and data handling were made by technicians Walter Judge, Richard Cheel, and Doug Schillinger at Dalhousie University, Jack Foley at Memorial University, and Rémi Desmarais at Institut Maurice Lamontagne, and we thank them all for their help. The work was supported by the Killam Foundation, the Natural Sciences and Engineering Research Council of Canada, the Canadian Foundation for Innovation, the Canadian Foundation for Climate and Atmospheric Sciences, and the Canadian Department of Fisheries and Oceans.

References

Bourgault, D. (2008), Shore-based photogrammetry of river ice, *Can. J. Civ. Eng.*, *35*(1), 80–86.

Bourgault, D., and D. E. Kelley (2003), Wave-induced boundary mixing in a partially mixed estuary, *J. Mar. Res.*, *61*(5), 283–296, doi:10.1357/002224003771815954.

Bourgault, D., and D. E. Kelley (2007), On the reflectance of uniform slopes for normally incident interfacial solitary waves, *J. Phys. Oceanogr.*, *37*, 1156–1162.

Bourgault, D., D. E. Kelley, and P. S. Galbraith (2005), Interfacial solitary wave run-up in the St. Lawrence Estuary, *J. Mar. Res.*, *63*, 1001–1015.

Bourgault, D., M. D. Blokhina, R. Mirshak, and D. E. Kelley (2007), Evolution of a shoaling internal solitary wavetrain, *Geophys. Res. Lett.*, *34*(L03601), doi:10.1029/2006GL028,462.

Bourgault, D., D. E. Kelley, and P. S. Galbraith (2008), Turbulence and boluses on an internal beach, *J. Mar. Res.*, *66*, 563–588.

Cyr, F., D. Bourgault, and P. S. Galbraith (2011), Interior versus boundary mixing of a cold intermediate layer, *J. Geophys. Res.*, *116*(C12), C12,029+, doi:10.1029/2011JC007359.

Davis, K. A., and S. G. Monismith (2011), The modification of bottom boundary layer turbulence and mixing by internal waves shoaling on a barrier reef, *J. Phys. Oceanogr.*, *41*(11), 2223–2241, doi:10.1175/2011JPO4344.1.

Elgar, S., B. Raubenheimer, and R. Guza (2005), Quality control of acoustic Doppler velocimeter data in the surfzone, *Measurement Science and Technology*, *16*, 1889.

Feddersen, F. (2010), Quality controlling surf zone acoustic doppler velocimeter observations to estimate the turbulent dissipation rate, *J. Atmos. Oceanic Technol.*, *27*(12), 2039–2055, doi:10.1175/2010JTECHO783.1.

Fischer, H., E. List, R. Koh, J. Imberger, and N. Brooks (1979), Mixing in Inland and Coastal Waters, Academic Press. San Diego Calif.

Gill, A. E. (1982), *Atmosphere-Ocean Dynamics*, *International geophysics series*, vol. *30*, 662 pp., Academic Press, New York.

Goring, D., and V. Nikora (2002), Despiking acoustic Doppler velocimeter data, *J. Hydraul. Eng.*, *128*, 117.

Green, M. O. (1992), Spectral estimates of bed shear stress at subcritical reynolds numbers in a tidal boundary layer, *J. Phys. Oceanogr.*, *22*(8), 903–917, doi:10.1175/1520-0485(1992)022<0903:SEOBSS>2.0.CO;2.

Groeskamp, S., J. Nauw, and L. Maas (2011), Observations of estuarine circulation and solitary internal waves in a highly energetic tidal channel, *Ocean Dynamics*, pp. 1–16.

Huntley, D. A. (1988), A modified inertial dissipation method for estimating seabed stresses at low reynolds numbers, with application to wave/current boundary layer measurements, *J. Phys. Oceanogr.*, *18*(2), 339–346, doi:10.1175/1520-0485(1988)018<0339:AMIDMF>2.0.CO;2.

Jay, D. A., and J. D. Smith (1990), Residual circulation in shallow estuaries 1. highly stratified, narrow estuaries, *J. Geophys. Res.*, *95*(C1), 711–731.

JCGM (2008), Evaluation of measurement data – Guide to the expression of uncertainty in measurement, Joint Committee for Guides in Metrology.

Kim, S.-C., C. T. Friedrichs, J. P.-Y. Maa, and L. D. Wright (2000), Estimating bottom stress in tidal boundary layer from acoustic Doppler velocimeter data, *J. Hydraul. Eng.*, *126*(6), 399–406, doi:10.1061/(ASCE)0733-9429(2000)126:6(399).

Klymak, J., and J. Moum (2003), Internal solitary waves of elevation advancing on a shoaling shelf, *Geophys. Res. Lett.*, *30*(20), 2045.

Lamb, K. (2003), Shoaling solitary internal waves: On a criterion for the formation of waves with trapped cores, *J. Fluid Mech.*, *478*, 81–100.

Lamb, K. G., and V. T. Nguyen (2009), Calculating energy flux in internal solitary waves with an application to reflectance, *J. Phys. Oceanogr.*, *39*(3), 559–580.

Mirshak, R. (2008), Interfacial internal waves impacting sloped boundaries, Ph.D. thesis, Dalhousie University, doi:Add data for field: Doi.

Mirshak, R., and D. Kelley (2009), Inferring propagation direction of nonlinear internal waves in a vertically sheared background flow, *J. Atmos. Ocean. Technol.*, *26*, 615–625, doi:10.1175/2008JTEC0632.1.

Monin, A., and A. Yaglom (1975), Statistical fluid mechanics II, MIT Press.

Moum, J. N., J. M. Klymak, J. D. Nash, A. Perlin, and W. D. Smyth (2007), Energy transport by nonlinear internal waves, *J. Phys. Oceanogr.*, *37*, 1968–1988.

Oakey, N. S. (1982), Determination of the rate of dissipation of turbulent energy from simultaneous temperature and velocity shear microstructure measurements, *J. Phys. Oceanogr.*, *12*, 256–271.

Quaresma, L., J. Vitorino, A. Oliveira, and J. da Silva (2007), Evidence of sediment resuspension by nonlinear internal waves on the western Portuguese mid-shelf, *Mar. Geol.*, *246*(2-4), 123–143.

Saucier, F., and J. Chassé (2000), Tidal circulation and buoyancy effects in the St.Lawrence Estuary. *Atmosphere-Ocean*, *38*(4), 505–556.

Scotti, A., B. Butman, R. Beardsley, P. Alexander, and S. Anderson (2005), A modified beam-to-earth transformation to measure short-wavelength internal waves with an acoustic Doppler current profiler, *J. Atmos. Oceanic Technol.*, *22*(5), 583–591.

Shroyer, E. L., J. N. Moum, and J. D. Nash (2009), Observations of polarity reversal in shoaling nonlinear internal waves, *J. Phys. Oceanogr.*, *39*(3), 691–701.

Shroyer, E., J. Moum, and J. Nash (2010a), Energy transformations and dissipation of nonlinear internal waves over New Jersey's continental shelf, *Nonlinear processes in Geophysics*, *17*, 345–360.

Shroyer, E. L., J. N. Moum, and J. D. Nash (2010b), Vertical heat flux and lateral mass transport in nonlinear internal waves, *Geophys. Res. Lett.*, *37*, L08601, doi:10.1029/2010GL042715.

SonTek (2001), SonTek ADVField Acoustic Doppler Velocimiter: Technical Documentation, San Diego, CA.

Soulsby, R. (1997), Dynamics of marine sands: a manual for practical applications, Thomas Telford.

Sreenivasan, K. (1995), On the universality of the Kolmogorov constant, *Phys. Fluids*, *7*(11), 2778–2784.

Stapleton, K., and D. Huntley (1995), Seabed stress determinations using the inertial dissipation method and the turbulent kinetic energy method, *Earth Surface Processes and Landforms*, *20*(9), 807–815.

Taylor, G. (1920), Tidal friction in the irish sea, *Philosophical Transactions of the Royal Society of London. Series A, Containing Papers of a Mathematical or Physical Character*, *220*, 1–33.

Tennekes, H., and J. Lumley (1972), A First Course in Turbulence, The MIT press.

Wang, C., and R. Pawlowicz (2011), Propagation speeds of strongly nonlinear near-surface internal waves in the Strait of Georgia, *J. Geophys. Res.*, *116*(C10), C10,021+, doi:10.1029/2010JC006776.

Zedel, L., A. Hay, R. Cabrera, and A. Lohrmann (1996), Performance of a single-beam pulse-to-pulse coherent Doppler profiler, *Oceanic Engineering, IEEE Journal of*, *21*(3), 290–297.